Accepted versión (28th July 2014) in Dalton Transactions 2014

Journal Name

RSCPublishing

ARTICLE

A-site sub-stoichiometry and oxygen vacancies as the origin of the electrical properties of $Sr_{2-y}LuNb_{1-x}Ti_xO_{6-\delta}$ perovskite-like materials.

Cite this: DOI: 10.1039/xoxxoooooox

Received ooth January 2012,
Accepted ooth January 2012

DOI: 10.1039/xoxxoooooox

www.rsc.org/

Z. Maupoey[a], M.T. Azcondo[a]*, J. C. Pérez-Flores[a], C. Ritter[b], K. Boulahya[c], U. Amador[a] and F. García-Alvarado[a]

Aliovalent substitution of Nb^{5+} by Ti^{4+} in Sr_2LuNbO_6 is limited to 10% of Nb atoms. A full structural determination by NPD confirms this and reveals that the structure is better described as a superstructure of the simple cubic perovskite (as previously reported) with monoclinic cell $2^{1/2}a_p x 2^{1/2}a_p x 2a_p$ and $\beta \approx 90^o$ (S.G. $P2_1/n$). The substituted materials present both: oxygen-vacancies induced as charge compensating and Sr-deficiency. Therefore, their formulae should be given as $Sr_{2-y}LuNb_{1-x}Ti_xO_{6-\delta}$. Electrical properties can be fully understood considering these compositional defects. The parent compound Sr_2LuNbO_6 presents low electrical conductivity in air, which improves by more than one order of magnitude by Ti substitution. In any case, the title oxides show low electrical conductivity in a wide oxygen partial pressure (pO_2) range (10^{-25} atm ≤ pO_2 ≤10^{-1} atm). At high pO_2 conductivity increases as pO_2 does due to oxygen-vacancies annihilation and holes creation, according to a general p-type semiconducting mechanism; A-site substoichiometry and Ti-substitution are at the origin of this behaviour. In the low pO_2 region, conductivity increases as oxygen partial pressure decreases. Reduction of cations, Nb^{5+} or Ti^{4+}, supports n-type conduction by electrons and oxygen vacancies creation. For the intermediate pO_2 range a low ionic conduction contribution is observed. Although the estimated ionic conductivity is not high in the substituted compounds, the strategy seems to be valid since a significant enhancement of ionic conduction is observed upon aliovalent substitution.

1 Introduction

Double perovskites $A_2BB'O_6$ have attracted for decades a considerable attention due to their interesting physical properties. A variety of properties can be adjusted due to the structural and chemical flexibility of the perovskite framework. Thus, subtle compositional changes such as: substitution in both A- and B-sites cations, anionic and cationic vacancies, as well as structural modifications, such as: cation ordering or anion ordering, cation displacements, octahedral tilting, etc [1] produce significant changes in the physical properties and, hence determine potential applications. In most cases a correct structural determination is needed to understand the structural details related to physical properties.

[a]Universidad CEU San Pablo, Facultad de Farmacia, Departamento de Química y Bioquímica, E-28668 Madrid, Spain.
[b]Institut Laue-Langevin. BP 156-38042 Grenoble Cedex 9, France
[c]Departamento de Química Inorgánica, Facultad Ciencias Químicas, Univ. Complutense, E-28040 Madrid, Spain.
*Corresponding Author. Tel.: +0034-91-3724715. E-mail: azcondo@ceu.es

Perovskite oxides have been extensively used in the development of new electrodes in both high- (SOFCs) and intermediate-temperature solid oxide fuel cells (IT-SOFCs).
Concerning SOFC applications, materials which present both mixed ionic-electronic conductivity (MIEC) and high catalytic activity are desirable as electrode materials. A simple strategy to improve the electronic conductivity is to induce mixed oxidation states in B-site ions, whereas oxide-ionic conduction can be enhanced through creation of oxygen anion vacancies. These effects can be achieved by appropriate aliovalent substitutions in the A- and/or B-metal sites. The bibliography shows several examples where these strategies are applied in perovskites as active SOFCs materials; for instance, as representative examples, (La, Sr) MnO_3 (LSM), (La, Sr) (Cr, Mn)O_3 (LSCM) and (La, Sr) (Ga, Mg)O_3 (LSGM) are very well-known materials for cathode, anode and electrolyte, respectively [2-7]
Although some problems arising from chemical compatibility, thermal mismatch, phase stability and others must be solved yet, perovskites-based materials can be used as whatever SOFC element (electrodes, electrolyte, interconnector); this possibility

let the development of the very appealing all-perovskite SOFC concept [5, 8, 9]

Although the use of rare-earth (RE) ions in perovskites is common, usually they play a structural role, remaining the possible electrochemical redox pair, M^{n+}/M^{n+1}, inactive. Alternative examples, where the rare-earth takes part in the electrochemical behaviour of the material, are particularly significant in AMO_3-based ceramics and related-doped ones (A=Ba, Sr, Ca; M=Pr, Zr, Ce) as ionic conductors.[10, 11]

In the development of new SOFC materials, we focus our studies on Sr_2RENbO_6 systems (RE = rare earth). Recently we published the first example of an electroceramic whose electrical conductivity under reducing conditions is due to the activation of the Eu^{3+}/Eu^{2+} redox pair. [12] In Sr_2EuNbO_6 aliovalent substitution of Nb^{5+} by Ti^{4+} is limited to 15%, but induces the corresponding oxygen vacancies as charge compensation mechanism. Even though the amount of such defect is very low, these vacancies produce a non-negligible oxide-ion conductivity (7.0 10^{-5} Scm^{-1} at 1123K). Besides, at low oxygen partial pressure n-type conductivity contribution was observed due to Eu^{2+} formation.

In order to tune both ionic and electronic contributions, and to assess the effect of RE-size on the oxygen ion mobility the synthesis of $Sr_2MNb_{1-x}Ti_xO_6$ compounds with some non-reducible trivalent rare-earth elements, (M= Nd, Y and Lu) has been attempted. Under our experimental conditions we only succeeded in partially replacing Nb by Ti to a detectable amount in the case of Lu. Thus we present in this paper a deep structural characterization of $Sr_2LuNb_{1-x}Ti_xO_{6-\delta}$, combined with magnetic and electrical measurements in order to explain its electrical properties on the basis of its defect-chemistry induced by doping and/or under different atmospheres.

2 Experimental

Samples of compositions $Sr_2LuNb_{1-x}Ti_xO_6$ ($0 \le x \le 0.2$) were prepared by a modified Pechini method. Stoichiometric quantities of Lu_2O_3 (99.99% Aldrich), $NbCl_5$ (99.9% Aldrich) and $SrCO_3$ (99.9% Merck) were solved in aqueous nitric solution. A 5% excess of the stoichiometric Sr-content was used in order to compensate the volatility of SrO. Then, high purity TiO_2 anatase (99.9% Aldrich) was added and stirred to obtain a homogeneous suspension. Citric acid was added under heating and vigorous stirring in a molar ratio of citric acid to metal ions of 3:1. To promote polymerization ethylene glycol (5mL) was added yielding a viscous resin. This resin was decomposed by continuous heating and stirring until ashes were formed. The obtained powder was burned at 1073K to remove organic matter. After milling and homogenization the powders were pressed into 13mm diameter pellets and fired at 1773K for 60h and cooled down to room temperature.

X-ray diffraction (XRD) patterns were recorded on a Bruker D8 high-resolution X-ray powder diffractometer, equipped with solid-state position-sensitive detector (PSD) LynxEye®, using monochromatic Cu $K_{\alpha 1}$ (λ= 1.5406 Å) radiation obtained with a germanium primary monochromator. Neutron powder diffraction (NPD) experiments at room temperature were performed on the high resolution diffractometer D2B at the Institut Laue-Langevin. A monochromatic beam of wavelength 1.5940 Å was selected with a Ge monochromator from the primary beam the divergence of which was defined by an additional 10' collimator to increase the instrumental resolution. The structural refinements were carried out by the Rietveld method using FullProf program [13]. The neutron scattering amplitudes used in the refinement were: 0.7020, 0.7054, -0.3438, 0.7210 and 0.5803 10^{-12} cm for Sr^{+2}, Nb^{+5}, Ti^{+4}, Lu^{+3} and O^{2-}, respectively; isotropic thermal factors (ITF) were used for all atoms. Constraints were employed throughout the refinement to keep the perovskite B-sites fully occupied and the same thermal factor for all oxygen atoms was assumed; on the contrary, occupation of A-site was refined.

Scanning electron microscopy (SEM) experiments were performed on sintered pellets using a FEI XL30® apparatus equipped with an EDAX® analyser for energy dispersive spectroscopy (EDS).

The samples were characterized by electron diffraction and high resolution electron microscopy (HREM) using a Jeol 3000 FEG electron microscope, fitted with a double tilting goniometer stage (±20°, ±20°). Local composition was analysed by energy-dispersive X-ray spectroscopy (EDS) with an Oxford analyser system attached to the above mentioned electron microscope. Simulated HREM images were calculated by the multislice method using the MacTempas software package. Electron energy loss spectroscopy (EELS) data were obtained from a Jeol 3000FEG transmission electron microscope operating at 300 kV, equipped with Enfina EELS attachment.

Magnetic measurements were performed using a superconducting quantum interference device magnetometer (Quantum Design, model MPMS-XL).

Impedance spectroscopy (IS) was done on dense pellets with both sides coated with platinum paint as electrodes, using a Solartron 1260 Frequency Response Analyser in the 1 MHz - 0.1 Hz range over the temperature range 298-1073 K in air.

Isothermal conductivity measurements as a function of pO_2 were performed on bars prepared by uniaxially pressing powders sintered at 1773K for 6 hours similarly as described in a previous work [14]. The cell was firstly equilibrated in a reducing atmosphere (5% H_2/Ar) for a minimum period of 12 hours; then the gas flow entrance was switched off and the chamber allowed to equilibrate slowly with the outside atmosphere over a period of several days, during which impedance measurements were registered every 0.25 increasing units of log pO_2 steps.

To measure the electronic conductivity of $Sr_2LuNb_{0.90}Ti_{0.10}O_6$ the electrode polarization technique based on Hebb-Wagner's procedure [15, 16] on dense pellets (relative density ≥ 92%) was attempted.

3 Results and discussion

3.1 Samples: composition and structure.

The structural details reported for the series of compounds Sr_2LnNbO_6, where Ln is a trivalent lanthanide ion (Ln: La-Lu) are scarce and somewhat contradictory. The oxide Sr_2SmNbO_6 was reported to adopt a monoclinic distortion of the perovskite structure (unit cell $2^{1/2}a_px2^{1/2}a_px2a_p$, being a_p the cell-parameter of the cubic perovskite, and S.G. $P2_1/n$(#14)) [17], as expected on the basis of the corresponding value of the tolerance factor (t=0.913). A similar structure model has been used to describe the compounds Sr_2YNbO_6 [18] (t=0.925) and Sr_2YbNbO_6 [19] (t=0.932). Concerning the Sr_2LnNbO_6 compounds with the small Ln ions, Sirotinkin et al. [17] proposed an orthorhombic distorted structure with S.G. P2nn (#34) (with same unit cell than that of the monoclinic structure) for Ln=Tm-Lu. This latter model was obtained from single-crystal X-ray diffraction data, which suggested a strong deformation of the octahedral framework, the octahedra no longer being rigid. However, at this point it must be stressed that, in spite of the general idea that single-crystal X-ray diffraction data are more suitable for structure determination and refinement than powder diffraction data, along the single-crystal data collection and reduction any microstructural information is missed. In some cases microstructure effects have to be taken into account to obtain a reliable structural model [20, 21]. Even more, in the paper by Sirotinkin et al. [17] many weak reflections not satisfying the systematic absences of the chosen S.G. were disregarded. As a result, a wrong symmetry was applied; this together with the low X-ray scattering power of oxygen yield to a wrong structure model which disagrees with what expected on the basis of the t-factors and with what observed along the whole series of Sr_2LnNbO_6 oxides. Indeed, as the size of the Ln^{3+} ion decreases the tolerance factor increases as a result of a better matching between the A-O and B-O distances and the structure becomes less distorted. Thus, there is no reason for the octahedra framework to be more distorted in the perovkites with smaller Ln^{3+} ions.

Bearing in mind these ideas, we developed a structural model for the compound $Sr_2LuNb_{1-x}Ti_xO_6$ ($0 \leq x \leq 0.2$) using XRD data which was confirmed for $Sr_2LuNb_{0.90}Ti_{0.10}O_6$ from NPD. Fig. 1 shows the XRD pattern for $Sr_2LuNb_{1-x}Ti_xO_6$ with x=0 which is similar to that one observed for Sr_2YbNbO_6. [19] In addition to the fundamental reflections of a typical simple cubic perovskite it shows several sets of extra peaks, pointing to a superstructure with a larger cell. Those fundamental reflections are clearly split at high diffraction angles, indicating a deviation from the cubic symmetry. For instance, the splitting of the $(222)_p$ simple-cubic-perovskite maximum into three, (see inset to Fig. 1), suggests a triclinic distortion of the aristotype cubic cell. This triclinic cell can be converted into a primitive monoclinic one with lattice parameters $2^{1/2}a_px2^{1/2}a_px2a_p$ and $\beta \approx 90^o$ which allows indexing all the observed peaks.

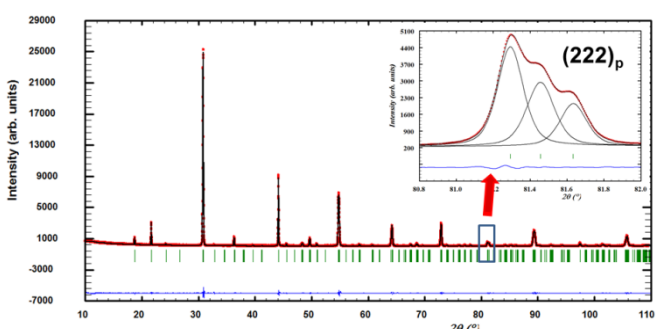

Figure 1: Experimental (red circles) and calculated (black continuous line) XRD patterns (and their difference, blue line at the bottom) for Sr_2LuNbO_6 assuming S.G. $P2_1/n$. The green vertical bars indicate the positions of the Bragg peaks. In the inset the splitting of the (222)p peak suggests a triclinic distortion of the cubic parent cell supporting the monoclinic cell used ($2^{1/2}a_px2^{1/2}a_px2a_p$, $\beta \approx 90º$).

Space-group determination using powder diffraction patterns is a rather difficult task, but this can be satisfactory accomplished considering the theoretical works previously reported on group-subgroup relationships in perovskites which considered not only rigid tilting of octahedral but also different kinds of metal ordering either in A-sites or B-sites. Thus, we succeeded in determining S.G. (#14) $P2_1/n$ as the most likely. Interestingly this is very common in monoclinic perovskites. This monoclinic distortion of the cubic aristotype is quite common in perovskite with rock-salt cationic ordering in the B-sites [1, 12, 22-26], resulting from the tilting of the BO_6 octahedra according to a scheme ($a^-a^-a^+$) [27]; the octahedra tilting being a mechanism to accommodate the mismatch between the A-O and B-O distances due to a small size of the A cation. [28]

The final structural parameters are given in Table SI 1 whereas selected structure information is shown in Table SI 2. A similar model can be used to fit the XRD data of $Sr_2LuNb_{1-x}Ti_xO_6$ (x=0.1, 0.2), the other compounds of the series. The corresponding XRD patterns are given in Figs. SI 1 and SI 2 and the refined parameters and structure information are included in Tables SI 1 and SI 2, respectively. Thus, as determined by XRD polycrystalline samples of composition $Sr_2LuNb_{1-x}Ti_xO_6$, ($0 \leq x \leq 0.2$) could be obtained as single-phase by the above described Pechini modified method.

Although XRD suggests that the substitution of Nb^{5+} by Ti^{4+} in $Sr_2LuNb_{1-x}Ti_xO_6$ is possible up to x=0.2, EDS analyses and images taken on the SEM microscopy clearly revealed that for x=0.2 segregation occurs. Thus, Fig. SI 3 demonstrates that the samples of nominal composition $Sr_2LuNb_{0.80}Ti_{0.20}O_6$ are not homogeneous. Phase separation has been observed in all the batches with this nominal composition. On the contrary, the samples with x=0.1 show no compositional inhomogeneity as evidenced in Fig. 2. All the samples prepared of nominal composition $Sr_2LuNb_{0.90}Ti_{0.10}O_6$ were confirmed to be single-phase by EDS, the actual chemical compositions being close to the nominal ones within the technique error (see Table 1). Even more, the distribution of all the constituting elements was confirmed to be homogeneous throughout the samples. Thus, Figures 2a and 2g show the back-scattered electron (BSE) images of a sample of the series $Sr_2LuNb_{1-x}Ti_xO_6$ with x=0.1, together with the corresponding element-distribution maps. Since the contrast in BSE images is sensitive to the average composition (light elements give dark contrasts, and vice-versa) Figures 2a and 2g already suggest a homogeneous compositions. This is confirmed by the element-distribution maps shown in figures 2b to 2f. Darker and brighter zones

observed in some of those images are artefacts due to the surface morphology (see Fig. 2h). Therefore, the limit of the aliovalent substitution of Nb^{5+} by Ti^{4+} in the title compounds is not high ($0.1 \leq x_{max} < 0.2$). We have studied the x=0.1 material more deeply by NPD prior to a detailed electrical characterization.

Table 1: Nominal and experimental (determined by EDS) compositions for $Sr_2LuNb_{0.90}Ti_{0.10}O_6$ (sample used for NPD and electrical characterization).

Element	Nominal composition (atom %)	Experimental composition (atom %)
Sr	20.00	20.6(3)
Lu	10.00	10.3(2)
Nb	9.00	8.2(3)
Ti	1.00	1.0(4)
O	60.00	59.9(3)

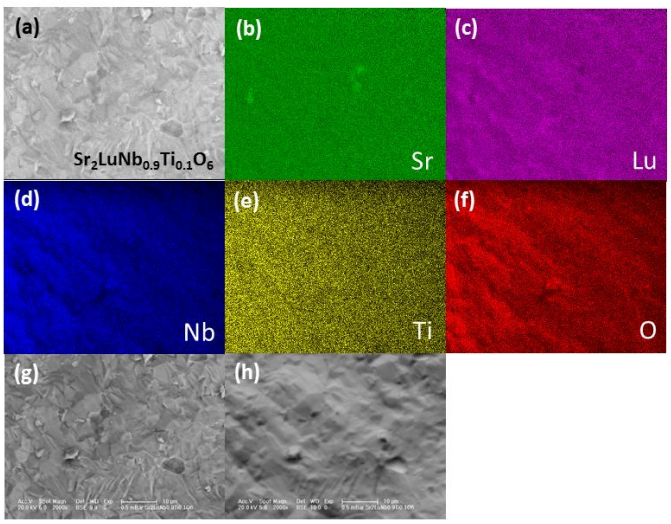

Figure 2: (a) Back-scattered electrons (BSE) image taken at a magnification of x 2000 and element-distribution maps of $Sr_2LuNb_{0.9}Ti_{0.1}O_6$ sample: (b) Sr, (c) Lu, (d) Nb, (e) Ti and (f) O. (g) and (h) BSE image and the corresponding topographic image, respectively showing the surface morphology responsible for some contrast effects in element-maps.

3.2 Crystal structure $Sr_2LuNb_{0.90}Ti_{0.10}O_6$

To confirm the partial substitution of Nb by Ti and the validity of the previously proposed structural model to describe $Sr_2LuNb_{0.90}Ti_{0.10}O_6$ material, HREM, EDS and EELS experiments were performed. Many crystals (about three dozens) were analysed on the transmission electron microscope; in all cases the composition was consistent with the nominal one within the experimental error. These analyses confirm that the elements are homogeneously distributed not only at microscopic level as suggested by SEM images (Fig. 2) but also at atomic scale. The sample homogeneity was also confirmed by EELS; Fig. SI 4 shows a typical spectrum.

Concerning the structure model HREM also gives crucial information. $Sr_2LuNb_{0.9}Ti_{0.1}O_6$ was studied by electron microscopy taking different zone axes in order to fully reconstruct the reciprocal/real space. In Fig. 3 the corresponding HREM micrograph shows an apparently well ordered material with d-spacing of 5.8 Å and 8.1 Å, corresponding to d_{100} and d_{001}. Fourier transform was performed on the HREM micrograph, looking for the existence of different domains that could evidence the presence of additional ordering of the structure. However, the whole crystal results homogeneous and only the maxima corresponding to the diagonal double perovskite unit cell were observed (Fig 3a). The contrast observed in this image consists of bright dots alternating with brightest ones, which can be associated to the Lu atoms alternating with Ti/Nb ones along [100] and [001]. Such contrast variation confirms that this material presents cationic ordering as proposed for the parent compound from XRD (Table SI 1) and confirmed by NPD for this Ti-contained derivative (see below).

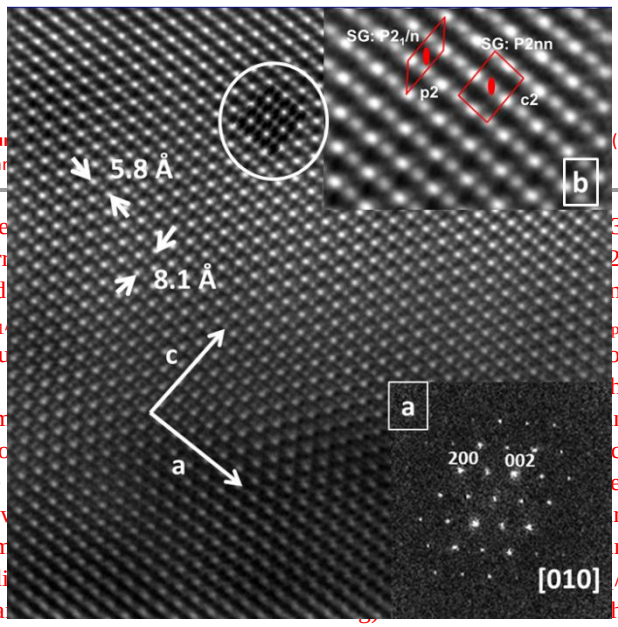

Figu (b) sym

The 3a cor 2n and nd $P2_1$ p). Thu on to he sym nt info ce the ed viev re sym re indi /n (tra he

orthorhombic S.G. P2nn. The only symmetry elements observed are two-fold axes perpendicular to the image plane, being the 2D groups p2 or c2 depending on the unit cell

election (in fact both plane groups are the same). This result discards the S.G. P2nn since the projection of this group along [010] presents c11m symmetry.

HREM micrographs were taken along other relevant directions. Thus, Fig. 4 demonstrates that crystals of $Sr_2LuNb_{0.90}Ti_{0.10}O_6$ are frequently twinned. Two domains oriented along [-110] and [001] with domain walls (010) are clearly observed. The corresponding FFT (Fig 4a and 4b) can be indexed with above mentioned unit cell. Unfortunately the observed reflection conditions are not consistent with those expected for either P2nn or $P2_1/n$ S.G.s; in particular 0k0 reflections should appear only for k=2n in both cases but k-odd maxima are observed by double diffraction. The presence of twinning and the fact that differences between these two S.G. are most likely due to subtle effects related with oxygen atoms make to discern the actual structure symmetry a very difficult task.

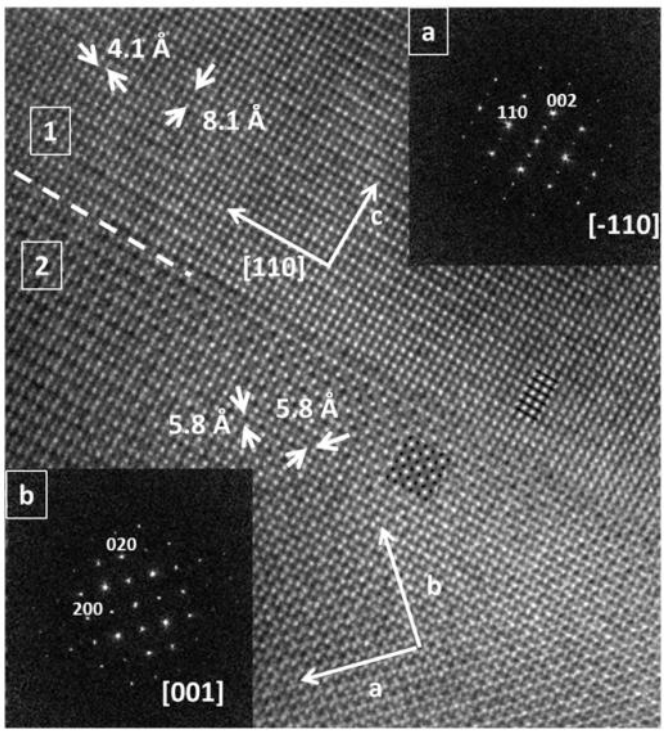

Figure 4. HREM image of $Sr_2LuNb_{0.9}Ti_{0.1}O_6$. Domain 1 along [-110], (a) corresponding optical FFT. Domain 2 along [001]. (b) corresponding optical FFT.

Neutron powder diffraction data confirm the structure of this oxide to be monoclinic (S.G. $P2_1/n$ (#14). The presence of peaks such as (120)/(210) and (140)/(410) (see Figs. 5 and SI 5) discards the model propose in ref [17]. Indeed, in S.G. P2nn (hk0) reflection with k+k=odd are forbidden whereas in $P2_1/n$ are not. Using the model described below, image calculations were performed. The simulated images (insets in Figs. 3 and 4) give a good fit to the experimental image viewed along different direction.

Table 2 collects the refined structural parameters of $Sr_2LuNb_{0.90}Ti_{0.10}O_6$ as obtained from NPD data; Fig. 5 shows the experimental, calculated and their difference NPD patterns. In Table 3 selected structural information is given.

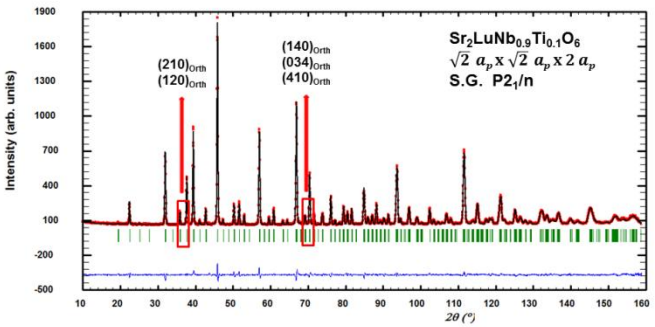

Figure 5: Experimental (red points), calculated (solid black line) and their difference (blue line at bottom) NPD patterns for $Sr_2LuNb_{0.9}Ti_{0.1}O_6$. The vertical bars (green) indicate the positions of the Bragg peaks.

Figure 6 shows schematic views of the room-temperature structure of these material based on data on Table 2. The darker smaller (grey) octahedra correspond to $(Nb/Ti)O_6$ whereas the lighter larger ones are LuO_6.

The structure consists of a framework of rigid BO_6 octahedra tilted according to the scheme ($a^-a^-a^+$) (Fig. 6) which is very common in either orthorhombic (S.G. Pnma) or monoclinic (S.G: $P2_1/n$ as in the present case) perovskites. [25, 26] The reason for the lower symmetry observed in cases as the herein reported is mainly due to the ordering of Lu and Nb/Ti in the B' and B'' positions of the structure (Table 2), the monoclinic angle being very close to 90 degrees (Table 2). In the orthorhombic model there is only one crystallographic site 4b (0 0 ½) for B cations, i.e. the symmetry does not allow for an ordered arrangement of the B cations. On the contrary, in the monoclinic model the 4b site in Pnma can be split into two independent crystallographic sites, 2d (½ 0 0) and 2c (½ 0 ½), which allow an ordered arrangement of the B cations (Fig. 6). Since the neutron scattering amplitudes of Ti is significantly different of those of Lu and Nb, the site occupancies can be readily identified. Refinements show that Nb^{5+} and Ti^{4+} share the B''-sites in a proportion close to the nominal one, whereas B'-sites are occupied by Lu^{3+}. Since these latter ions are significantly larger ($^{VI}r(Lu^{3+})$= 0.861 Å) than Nb^{5+} and Ti^{4+} ($^{VI}r(Nb^{5+})$= 0.64 Å, $^{VI}r(Ti^{4+})$= 0.605 Å) no intermixing or anti-site defects (AS) occur, thus small Ti and Nb cations share B''-sites and large Lu^{3+} ions occupy B'-positions. It is well established that B-site cation ordering is enhanced when the ionic size and/or charge difference of the B-ions are large [1]. This ordering result in cation-anion bond lengths associated to each of the two B-cations (Nb^{5+}/Ti^{4+}) and Lu^{3+} which are necessarily different (Table 3). Therefore, the volumes of corner-sharing octahedra are also different as shown in Table 3. Bond valence sums also confirm the cation ordering in the perovskite B-sites.

Table 2: Structural parameters for $Sr_2LuNb_{0.90}Ti_{0.10}O_6$ obtained from NPD data.

Space Group [a]	$P2_1/n$		
a (Å)	5.7626(1)		
b (Å)	5.7801(1)		
c (Å)	8.1552(2)		
β (deg)	90.080(2)		
Volume (Å^3)	271.62(1)		
Sr position	**4e**	**O(1) position**	**4e**
Occ Sr	0.986(6)	x	0.2256(6)
x	0.5038(6)	y	0.2030(6)
y	0.5235(2)	z	-0.0368(6)
z	0.2476(6)	Occ	0.985(2)
U*100 (Å^2)	0.54(2)	U*100 (Å^2)	0.53(4)
B' position	**2c**	**O(2) position**	**4e**
Occ Lu	0.50	x	0.2943(6)
U*100 (Å^2)	0.04(1)	y	0.7264(5)
B'' position	**2d**	z	-0.0368(5)
Occ Nb/Ti	0.901(2)/0.0992)	Occ	0.985(2)
U*100 (Å^2)	0.50(2)	U*100 (Å^2)	0.53 (4)
		O(3) position	**4e**
		x	0.4307(4)
		y	-0.0156(4)
		z	0.2398(5)
		Occ	0.985(3)
		U*100 (Å^2)	0.53(4)

[a] $P2_1/n$ (#14): 4e (xyz), 2d (½ 0 0), 2c (0 ½ 0c)
χ^2= 4.21, R_{wp}= 4.60%, R_{exp}= 2.24%, R_B= 3.33%,
Composition: $Sr_{1.97(1)}LuNb_{0.901(2)}Ti_{0.099(2)}O_{5.91(2)}$

The mismatch between the A-O and B-O distances, evidenced by a value of the t-parameter below unity (t=0.956), induces a co-operative tilting of the B'O_6 and B''O_6 octahedra to accommodate Sr^{2+} ions which are too small for the A-site cavity. The tilting scheme is confirmed to be ($a^-a^-c^+$) in the Glazer notation [27], indicating that the octahedra rotate along the Cartesian axes x and y in consecutive layers in opposite directions whereas along the z-axis they rotate in the same direction as is clearly shown in Figs. 6a-6c. The octahedra tilts can be calculated from the B'-O-B'' bond angles (ω) as (180-ω)/2; the values obtained from NPD are given in Table 3. The in-phase and out-of-phase tilting angles are similar about 11 degrees, in spite of the large different of the octahedra size that could induce noticeable differences in the tilting angles as a result of their distortions [19]. In our case, both B'O_6 and B"O_6 octahedra are noticeable distorted (as indicated by the corresponding parameters in Table 3), but in a similar extent; thus no relevant differences in the tilt angles arise. It is worth noting that usually, the larger the B-cations the larger the distortion of the BO_6 octahedra since for energetic and geometrical reasons deformation of large M-O bonds is favored. However, in $Sr_2LuNb_{0.90}Ti_{0.10}O_6$ both LuO_6 and (Nb/Ti)O_6 octahedra are similarly distorted; even more, the smaller (Nb/Ti)O_6 octahedra are slightly more distorted. This seems to be a result of the accommodation of two different cations (Nb^{5+} and Ti^{4+}) with different sizes and charges in the same crystallographic position.

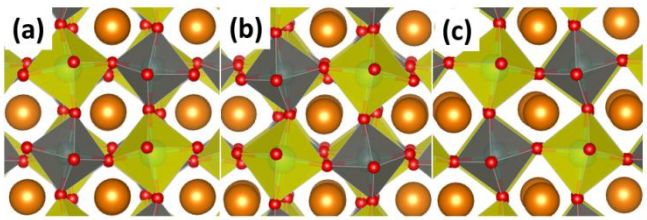

Figure 6: Schematic views of the structure of $Sr_2LuNb_{0.90}Ti_{0.10}O_6$ along the three perovskite main directions equivalent in the monoclinic cell to [110] (a), [-110] (b) and [001] (c). The dark small octahedra (grey in color) correspond to (Nb/Ti)O_6 and the light (yellow) larger ones to LuO_6.

NPD data of $Sr_2LuNb_{0.90}Ti_{0.10}O_6$ revealed two important structural features concerning the actual (refined) material's composition, $Sr_{1.97(1)}LuNb_{0.901(2)}Ti_{0.099(2)}O_{5.91(2)}$, which are relevant for understanding its electrical properties.

First, this oxide presents A-site vacancies: when refined the occupancy of the Sr-positions results slightly, but significantly, below 100%. This A-site off-stoichiometry was not reported for other non-substituted members of the Sr_2LnNbO_6 series [17-19]; thus it could be associated to the aliovalent substitution of Nb^{5+} by Ti^{4+}, though there is no evident explanation for this.

Second, it contains a significant amount of oxygen vacancies.

Table 3: Selected structural information for $Sr_2LuNb_{0.90}Ti_{0.10}O_6$ obtained from NPD data. Angles are given in degrees and distances in Å; distortion Δ of the BO_n polyhedra and Bond Valence Sums [29], are reported as $\Delta=1/n\ \Sigma_{j=1,n}$ [12] where <d> is the average B-O distance. The quadratic elongation λ is given by $\lambda=\Sigma_{j=1,n}(l_i/l_0)^2/n$ and the bond-angle variance σ is given by $\sigma=\Sigma_{j=1,n}(\theta_i-\theta_0)^2/(n-1)$ where l_0 and θ_0 are the cation-anion bond lengths and cation-anion-cation bond angles in regular coordination polyhedra, respectively, and l_i and θ_i are the cation-anion bond lengths and cation-anion-cation bond angles of the ith bond [30]

[a] Tilt angle θ	11.0(1)		
[b] Tilt angle φ	11.3(1)		
[c] Tilt angle μ	114(1)		
	LuO_6 octahedron		(Nb/Ti) O_6 octahedron
B'-O(1) x 2	2.171(4)	B''-O(1) x 2	1.987(4)
B'-O(2) x 2	2.163(4)	B''-O(2) x 2	1.999(4)
B'-O(3) x 2	2.161(5)	B''-O(3) x 2	1.999(5)
Average B'-O	2.165(4)	Average B''-O	1.995(4)
Octahedron volume (Å^3)	13.5218	Octahedron volume (Å^3)	10.5810
Distortion B'-O_6 x 10^4	17.7	Distortion B'-O_6 x 10^4	25.4
Quadratic elongation	1.0003	Quadratic elongation	1.0002
Bond angle variance	0.9583 deg^2	Bond angle variance	0.8171 deg^2
BVS	3.56(1)	BVS	4.80(2)

[a] With [110], [b] With [1-10], [c]With [001]

The relationship between the aliovalent substitution and oxygen-vacancies creation is much more straightforward. Indeed, two mechanisms can be though to compensate the positive charge lost when Nb^{5+} is replaced by Ti^{4+}: a) the oxidation of a cation present in the material and b) the creation of oxygen vacancies. Since in the parent Sr_2LuNbO_6 all the cations are in their highest oxidation states, the loss of positive charge due to the aliovalent substitution can be only compensated by a decreasing of negative charge, i.e. by creation of anion vacancies (Eq. [1]). In addition, the presence of Sr-vacancies also may contribute to the formation of anion vacancies (Eq. [2]), thus the concentration of oxygen-vacancies is noticeably high due to [1] + [2].

$$x\ TiO_2(Sr_2LuNbO_6) \longrightarrow x\ Ti'_{Nb} + x/2\ V_O^{\bullet\bullet} + Sr_2LuNb_{1-x}Ti_xO_{6-x/2} \quad [1]$$

$$(Sr_2LuNb_{1-x}Ti_xO_{6-x/2}) \longrightarrow y\ V''_{Sr} + y\ V_O^{\bullet\bullet} + Sr_{2-y}LuNb_{1-x}Ti_xO_{6-x/2-y} + y\ SrO \quad [2]$$

As will be discussed below, both the low Sr-deficiency (0.03 p.f.u.) and the high amount of oxygen vacancies (0.09 p.f.u.) play important roles in the electrical properties of this material.

3.3 Electrical properties.

Figure 7 shows the Arrhenius plots of total conductivity determined by IS for x= 0 and 0.1. Both samples exhibit similar semiconducting behaviours. The partial replacement of 10% of niobium by titanium noticeably improves conductivity. For example, it increases from $7.7\cdot10^{-5}$ to $3.5\ 10^{-4}$ Scm^{-1} at 1073K; this difference is even more pronounced at lower temperatures. Besides, the activation energy decreases from 0.96 to 0.67 eV, still in the range of typically ionic crystals. However, the decreasing of activation energy upon substitution seems to point to a change in nature of carriers, likely dominated by intrinsic defect in the parent material and by extrinsic defects in the Ti-substituted ones. On the other hand, conductivity of the sample with x=0.2 (not shown) exhibits very close behaviour and magnitude than that of the sample with x=0.1. This supports the previously discussed results that showed the limit for aliovalent substitution to be x=0.1; whereas phase segregation occurs for x=0.2. The increasing of total conductivity with Ti-content is due to enhancement of both bulk and grain boundary conductions as depicted in the corresponding Arrhenius plots (Figs. SI 6 and SI 7). Similarly, a lowering of activation energies of both bulk and grain boundaries upon substitution is also observed. Considering that aliovalent substitution induces oxygen vacancies, the enhancement of conductivity can be ascribed to improvement of ionic conductivity associated to such a type of defects.

Therefore, to further investigate this hypothesis and the possible participation of other defects, the dependence of conductivity on oxygen partial pressure (pO_2) has been studied. IS measurements under the different atmospheres, dry air and wet air (H_2O and D_2O) at 673-1173 K did not show any significant changes in total conductivity. Therefore, significant proton conductivity is discarded as it was the case of the homologous $Sr_2EuNb_{1-x}Ti_xO_{6-x/2}$compound.[12]

Figure 8 illustrates the pO_2 dependence of total conductivity at 1173 K for $Sr_2LuNb_{0.90}Ti_{0.10}O_{6-\delta}$ ($0 \le x \le 0.1$). These two compositions exhibit a similar behaviour in as much as two clearly distinctive branches of conductivity dependence on pO_2 are found.

Conductivity increases with oxygen partial pressure in the high pO_2 region (from 10^{-5} atm to ambient pressure) whereas the opposite happens in the low pO_2 region (below 10^{-15} atm); the former is assigned to *p*-type whereas the latter is due to *n*-type conduction.

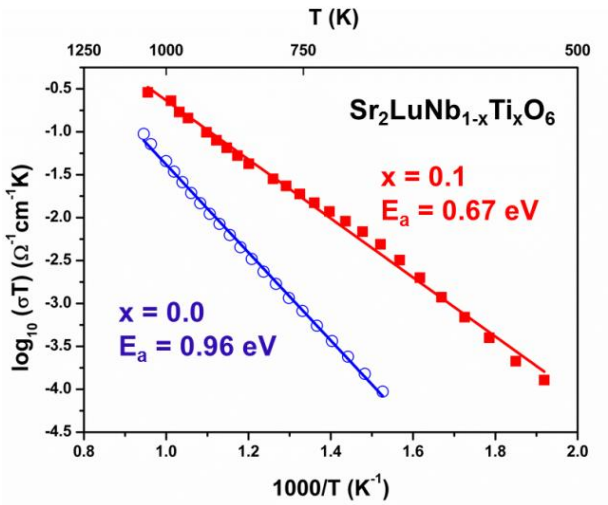

Figure 7. Arrhenius plots showing the temperature dependence of the total conductivity of $Sr_2EuNb_{1-x}Ti_xO_6$ (x=0 and 0.1). Activation energies are also indicated.

The existence of *p*-type conduction at high pO_2 confirms the presence of oxygen vacancies in the x=0.1 series member, whose actual composition is $Sr_{1.97(1)}LuNb_{0.901(2)}Ti_{0.099(2)}O_{5.91(2)}$, as determined by means of NPD data refinement. This composition suggests two possible mechanisms for anion-vacancies creation: aliovalent substitution (Nb^{5+} by Ti^{4+}) and Sr-deficiency (Sr sub-stoichiometry). Therefore, it should not be unexpected that the latter effect may be also present in the parent oxide, Sr_2LuNbO_6, giving rise to *p*-type conduction if one assumes a more realistic chemical composition as $Sr_{2-y}LuNbO_{6-y/2}$. Indeed, A-cationic deficiency is a well-established and understood phenomenon in perovskites [1].

Regardless the origin of oxygen vacancies, conductivity increases as oxygen partial pressure increases due to defects annihilation accordingly to the equilibrium equation given in [3]:

$$V_O^{\bullet\bullet} + \tfrac{1}{2}O_2 \leftrightarrow O_O^x + 2h^{\bullet} \qquad [3]$$

From this, equation [4] can be deduced to account for electronic conductivity:

$$\sigma_{elec} \propto [h^{\bullet}] = K_e^{1/2}[V_O^{\bullet\bullet}]^{1/2}(pO_2)^{1/4} \qquad [4]$$

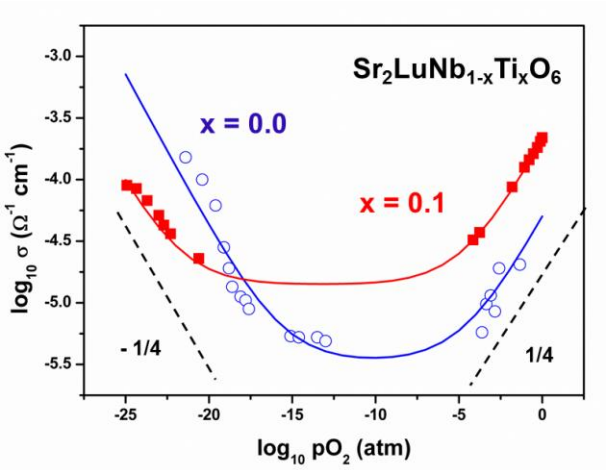

Figure 8. Dependence of the total conductivity for $Sr_2LuNb_{1-x}Ti_xO_6$ (x=0 and 0.1) with pO_2 to 1173K. Dashed lines with slopes ¼ and -¼ are included as guides for the eyes.

If the concentration of extrinsic vacancies, those originated by Ti-substitution, is much larger than those annihilated as pO_2 increases, $[V_O^{\bullet\bullet}]$ can be considered as a constant and a power law $(pO_2)^{1/4}$ dependence of conductivity must be observed. This is effectively the case of the sample with nominal composition $Sr_2LuNb_{0.90}Ti_{0.10}O_{6-\delta}$ (Fig. 8). In the case of $Sr_{2-y}LuNbO_{6-\delta}$ such dependence is less clear, since the concentration of oxygen vacancies is smaller and the assumption that $[V_O^{\bullet\bullet}]$ remains constant upon pO_2 changes might not be valid. In any case it is interesting to note that accordingly to Eq. [4], *p*-type electronic conductivity is higher in $Sr_2LuNb_{0.90}Ti_{0.10}O_{6-\delta}$ because $[V_O^{\bullet\bullet}]$ is expected to be also higher.

On the other hand, the existence of a *n*-type branch in the low pO_2 region (below 10^{-15} atm) can be associated to the presence of reducible cations mainly Nb^{5+} and Ti^{4+}. In this connection , the Eu^{3+}/Eu^{2+} pair in the similar $Sr_2EuNb_{1-x}Ti_xO_{6-\delta}$ series plays a crucial role in its *n-type* semiconducting behaviour.[12] Thus, in the title materials, reduction of Lu^{3+} should not be discarded, even though Lu^{3+} is not as easily reducible as Eu^{3+}. Note that Lu_2O_3 is the only lutetium-containing oxide that has been reduced so far. The concentration of oxygen-vacancies and Lu^{2+} ions are very low but render this oxide strongly coloured.[31, 32] Since we observed no colour change in our samples when heated under reducing conditions (5% H_2/Ar to 1173K during 24h) no reduction of Lu^{3+} to Lu^{2+} is expected. Furthermore, magnetic measurements carried out at room temperature on these samples revealed a diamagnetic behaviour and therefore the absence of paramagnetic cations, i.e., Lu^{2+}, Nb^{4+} and Ti^{3+} to a significant amount.

Regardless the active redox-pair $M^{n+}/M^{(n-1)+}$, the same equilibrium defects has to be proposed for both samples in order to justify the conductivity dependency at low pO_2 (Fig. 8). Thus Eq. [5] represents oxygen vacancies and electrons formation upon reduction:

$$O_O^x \leftrightarrow \frac{1}{2}O_2 + V_O^{\bullet\bullet} + 2e' \quad [5]$$

From Eq. [5], the corresponding mass action equation gives:

$$\sigma_{elec} \propto [e'] = K_e^{1/2} [V_O^{\bullet\bullet}]^{-1/2} (pO_2)^{-1/4} \quad [6]$$

As shown in Fig. 8, a $(pO_2)^{(-1/4)}$ power-law dependence of conductivity is observed for both the parent and Ti-containing samples in the low-pO_2 ranges suggesting that oxygen vacancies created upon reduction are negligible; thus, $[V_O^{\bullet\bullet}]$ can be considered as a constant in Eq [6]. The limited extent of oxygen vacancies created upon reduction agrees with the result of magnetic measurements on reduced samples; the extremely low concentration of reduced paramagnetic ions (and the concomitant additional oxygen vacancies) precludes its detection by that technique. However, such a small amount of reduced ions has a paramount influence on electrical properties. In the intermediate oxygen partial pressure, the parent and Ti-substituted samples exhibit similar and low conductivity (ca. 10^{-5} $\Omega^{-1}cm^{-1}$). Having into account that Ti^{4+} is easier to reduce than Nb^{5+}, the absence of significant amount of Ti^{3+} indicates that the extrinsic vacancies concentration created by the aliovalent substitution is close to the maximum that the structure can tolerate and further reduction is not easy to attain, even though reducible cations are present. In this pO_2 range the total conductivity of the x=0.1 sample remains constant; this behaviour is ascribed to an ionic conduction mechanism due to mobile oxygen vacancies. Again, this points to the aliovalent substitution (Nb^{5+} by Ti^{4+}) as the responsible for the existence of such anion vacancies. On the other hand, for x=0, the ionic conductivity is not as clearly observed as in the substituted compound, due to the relative magnitudes of electronic and ionic contributions. Anyhow, as the Sr-substoichiometry originates oxygen vacancies, consequently ionic conductivity is expected. Thus, a similar behaviour is assumed for both samples and the experimental data were fitted to the empirical equation given in [7] in order to estimate the different contributions to the total conductivity:

$$\sigma_{total} = \sigma_i^\circ(pO_2)^\circ + \sigma_p^\circ (pO_2)^n + \sigma_n^\circ (pO_2)^m \quad [7]$$

where σ_i°, σ_p° and σ_n° are the ionic, *p*-type and *n*-type contributions extrapolated to pure oxygen condition, respectively. The continuous lines in Fig. 8 correspond to the best fits using the final parameters given in Table 4. The exponents, n and m, are kept constant, equal to ¼ and -¼, respectively, since these are physically-meaning values close to the experimentally determined for both samples. Ionic conductivity increases by one order of magnitude upon titanium substitution reaching a value of $1.0 \cdot 10^{-5}$ Scm^{-1} for x=0.1. This demonstrates a significant mobility of oxide ions in the structure of this double perovskite as it was previously observed in the case of the Eu homologous.[12]

Instead of estimating the ionic conductivity, it would be possible to experimentally determine the electronic conductivity, and from here oxygen ionic conductivity, using the DC polarisation technique (ion-blocking) as we previously reported in the case of $Sr_2EuNb_{0.85}Ti_{0.15}O_{6-\delta}$ (σ_i= 7.0(5) 10^{-5} S/cm). However, the expected ionic conductivity for $Sr_2LuNb_{0.9}Ti_{0.1}O_{6-\delta}$, (Table 4) is even lower. Thus though, ion-blocking measurements have been carried for different dense pellets of the x=0.1 sample, it was not possible to obtain reliable data on electronic conductivity at different polarization steps. For such a low oxygen conductivity, the extension of oxygen ion migration from one side to the other of the cell is limited and measured current steady-state was not reached

.

Table 4. Refined parameters for the fitting of the experimental conductivity to Eq.[7] where σ_i°, σ_p° and σ_n° refer to the ionic, *p*-type and *n*-type contributions extrapolated to pure oxygen condition to total conductivity, respectively.

Nominal composition	σ_i^o (Scm^{-1})	σ_p^o (Scm^{-1})	σ_n^o (Scm^{-1})
Sr_2LuNbO_6	$1.5 \cdot 10^{-6}$	$5.0 \cdot 10^{-5}$	$5.0 \cdot 10^{-10}$
$Sr_2LuNb_{0.9}Ti_{0.1}O_{6-\delta}$	$1.0 \cdot 10^{-5}$	$2.4 \cdot 10^{-4}$	$6.0 \cdot 10^{-11}$

Nevertheless, the refined value in Table 4 (σ_i= 1.0 x 10^{-5} Scm^{-1}) confirms the non-negligible but low contribution of oxygen ion conduction in this material. The value of $Sr_2LuNb_{0.9}Ti_{.0.1}O_{6-\delta}$ conductivity is too low to make this material potentially useful. However, the demonstration of oxide-ion conductivity opens the possibility of improving such properties by increasing substitution percentage of Nb. The case is similar to the homologous oxides $Sr_2EuNb_{1-x}Ti_xO_{6-x/2}$ previously reported.[12] However, the replacing of Eu by Lu shifts the ionic conductivity to lower values, ca. one order of magnitude. Additionally, n-type contribution to conductivity is shifted to lower pO_2, below 10^{-20} atm, revealing a different role of the rare earth in both cases. As a consequence a wider pO_2 range is dominated by ionic conduction in the $Sr_{2-y}LuNb_{1-x}Ti_xO_{6-\delta}$ series.

4 Concluding remarks

Perovskite-like oxides with nominal compositions $Sr_2LuNb_{1-x}Ti_xO_{6-\delta}$ series have been synthesized as new oxide-ion conducting materials. Aliovalent substitution of Nb^{5+} by Ti^{4+} is limited to 10% as determined by powder XRD and SEM; oxygen-vacancies are induced as charge compensating mechanism. This was confirmed by a detailed structural characterization using NPD that also reveals that the structure should be described as a superstructure of the simple cubic

perovskite (as previously reported) with monoclinic cell $2^{1/2}a_p x 2^{1/2}a_p x 2a_p$ and $\beta \approx 90^o$ (S.G. $P2_1/n$). Additionally, these materials show Sr-deficiency. Therefore, their formulae should be given as $Sr_{2-y}LuNb_{1-x}Ti_xO_{6-\delta}$.

Electrical properties can be fully understood considering these compositional defects. The parent compound Sr_2LuNbO_6 presents low electrical conductivity in air, which improves by one order of magnitude in the substituted compound, (from $7.7 \cdot 10^{-5}$ to $3.5 \cdot 10^{-4}$ S cm^{-1} at 1073K). Low electrical conductivity is also observed for the title oxides in the whole oxygen partial pressure measured (10^{-25} atm $\leq pO_2 \leq 10^{-1}$ atm). At high pO_2 conductivity increases as pO_2 does due to oxygen-vacancies annihilation and holes creation, according to a general p-type semiconducting mechanism; A-site sub-stoichiometry and Ti-substitution are at the origin of this behaviour.

In the low pO_2 region, conductivity increases as oxygen partial pressure decreases. Reduction of cations, Nb^{5+} or Ti^{4+}, supports n-type conduction by electrons and oxygen vacancies creation. However, the concentration of reduced ions is very low as evidenced by magnetic measures. For intermediate pO_2 range electrical transport presents a significant ionic contribution. The ionic conductivity estimated according to a general mixed conduction model and ion-blocking measures is low in both the parent and the Ti-substituted materials. However, aliovalent replacement appears as a valid strategy to improve ionic conduction since a significant enhancement is observed upon substitution.

Acknowledgements

We thank the Ministerio de Economía y Competitividad (MINECO) and Comunidad de Madrid for funding the projects MAT2010-19837-C06 and S2009/PPQ-1626, respectively. Financial support from Universidad San Pablo is also acknowledged. Access to the neutron facilities at the Institut Laue Langevin is gratefully acknowledged. Z. Maupoey thanks Ministerio de Ciencia e Innovación and ESF of the European Commission for funding the predoctoral grant BES-2008-008236.We thank also to Dr. Julio Romero de Paz by the Magnetic measurements.

†Figure SI 1: Experimental (red circles) and calculated (black continuous line) XRD patterns (and their difference, blue line at the bottom) for $Sr_2LuNb_{0.90}Ti_{0.10}O_6$ assuming S.G. $P2_1/n$. The green vertical bars indicate the positions of the Bragg peaks. Figure SI 2: Experimental (red circles) and calculated (black continuous line) XRD patterns (and their difference, blue line at the bottom) for $Sr_2LuNb_{0.80}Ti_{0.20}O_6$ assuming S.G. $P2_1/n$. The green vertical bars indicate the positions of the Bragg peaks. Figure SI 3: (a) Back-scattered electrons (BSE) image taken at a magnification of x 2000 and element-distribution maps of $Sr_2LuNb_{0.80}Ti_{0.20}O_6$ sample: (b) Sr, (c) Lu, (d) Nb, (e) Ti and (f) O. Figure SI 4: EELS spectra of the $Nb_{M3,2}$, $Ti_{L3,2}$, O_k edges for $Sr_2LuNb_{0.90}Ti_{0.10}O_6$. Figure SI 5: Enlarged plot of the NPD zone where Bragg peaks (a) (120)/(210) and (b) (140)/(410) appear. These maxima are not compatible with S.G. P2nn previously proposed for Sr_2LuNbO_6 (Sirotinkin, V.P., Efremov, V.A., Trunov, V K.; The crystal structures of Sr_2SmNbO_6 and Sr_2TmNbO_6., Russian Journal of Inorganic Chemistry 1985, 30(7), 981-983). Figure SI 6: Arrhenius plots showing the temperature dependence of the bulk conductivity of $Sr_2EuNb_{1-x}Ti_xO_6$ (x=0 and 0.1). Activation energies are also indicated. Figure SI 7: Arrhenius plots showing the temperature dependence of the grain boundary conductivity of $Sr_2EuNb_{1-x}Ti_xO_6$ (x=0 and 0.1). Activation energies are also indicated. Table SI 1: Structural parameters for $Sr_2LuNb_{1-x}Ti_xO_6$ compounds obtained from XRD. Table SI 2: Selected structural information for $Sr_2LuNb_{1-x}Ti_xO_6$ compounds obtained from XRD data. Angles are given in degrees and distances in Å.

Notes and References

1. R. H. Mitchell, *Perovskite: Modern and Ancient*, Ontario (Canada), 2002.
2. J. Mizusaki, Yonemura,Y. , Kamata,H. , Ohyama,K. , Mori,N. , Takai,H. , Tagawa,H. , Dokiya,M. , Naraya,K. ; Sasamoto,T. , Inaba,H. , HashimotoT. , *Solid State Ionics*, 2000, **132**, 167.
3. S. Miyoshi, Hong,J.-O., Yashiro,K. , Kaimai,A., Nigara,Y., Kawamura,K., Kawada,T., Mizusaki,J., *Solid State Ionics*,, 2002, **154-155**, 257.
4. J. Sfeir, Buffat,P. A. , Möckli,P. , Xanthopoulos,N. , Vasquez,R. , Mathieu,H. J. , Herle,J.V, Thampi,K. R., *J. Catal.*, 2001, **202**, 229.
5. S. Tao, Irvine, J. T. S. , Kilner, J. A. , *Adv. Mater*, 2005, **17**, 1734.
6. H. Ishihara, Matsuda, Y., Takita,J,, *J. Am. Chem. Soc*., 1994, **116**, 3801.
7. H. Ishihara, Matsuda, Y., Takita,J,, *Solid State Ionics*, 1995, **79**, 147.
8. J. Peña-Martínez, Marrero-López, D, Ruiz-Morales,J. C. , Savaniu, C. , Nuñez, P. , Irvine, J. T. S. , *Chem. Mater*. , 2006, **B18B**, 1001.
9. A. Atkinson, Barnett,S. , Gorte,R. J. , Irvine,J. T. S. , McEvoy,A. J. , Mogensen,M. , Singhal,S. C., Vohs, J. , *Nature Mater*. , 2004, **3**, 17.
10. H. Uchida, Maeda,N. , Iwahara,H. , *Solid State Ionics*, 1983, **11**, 117.
11. N. Taniguchi, Hatoh,K. , Niikura,J. Gamo,T. , *Solid State Ionics*, 1992, **53-56**, 998.
12. Z. Maupoey, M. T. Azcondo, U. Amador, A. Kuhn, J. C. Perez-Flores, J. R. de Paz, N. Bonanos and F. Garcia-Alvarado, *Journal of Materials Chemistry*, 2012, **22**, 18033-18042.
13. J. Rodríguez-Carvajal, *Physica B: Condensed Matter*, 1993, **192**, 55-69.
14. J. C. Perez Flores, C. Ritter, D. Perez-Coll, G. C. Mather, F. Garcia-Alvarado and U. Amador, *Journal of Materials Chemistry*, 2011, **21**, 13195-13204.
15. C. Wagner, *Proceedings of 27th Meeting of the International Comittee on Electrochemical, Thermodinamics and Kinetics, Lindau, 1955*, Butterworths Scientific Publication, London, 1957.
16. M. H. Hebb, *J.Chem. Phys*, 1952, **20**, 185.
17. V. P. E. Sirotinkin, V.A.;Trunov, V.K.,, *Russian Journal of Inorganic Chemistry*, 1985, **30**, 1727-1730.
18. C. J. B. Howard, P.W.;Kennedy, B.J.;Woodward, P.M.,, *Acta Crystallographica B*, 2005, **39**, 1983.
19. W. K. C. Jae Ho Yang, Jin Ho Lee, Chang Hee Lee, *Acta crystallographica B*, 1999, **55**, 348-354.

20. S. García-Martín, Alario-Franco, M.A., Ehrenberg, H., Rodríguez-Carvajal, J., Amador, U., *Journal of the American Chemical Society*, 2004, **126**, 3587-3596.
21. A. Vegas, M. Vallet-Regi, J. M. Gonzalez-Calbet and M. A. Alario-Franco, *Acta Crystallographica Section B*, 1986, **42**, 167-172.
22. P. Woodward, *Acta Crystallographica Section B*, 1997, **53**, 44-66.
23. P. Woodward, *Acta Crystallographica Section B*, 1997, **53**, 32-43.
24. A. Gómez-Pérez, Yuste, M.,Pérez-Flores, J.C.,Ritter, C., Azcondo, M.T., Canales-Vázquez, J., Gálvez-Sánchez, M.,Boulahya, K.,García-Alvarado, F., Amador, U., *Journal of Power Sources*, 2013, **227**, 309-317.
25. J. C. Pérez-Flores, Ritter, C., Pérez-Coll, D., Mather, G. C., Canales-Vázquez, J., Gálvez-Sánchez, M., García-Alvarado, F., Amador, U., *International Journal of Hydrogen Energy*, 2012, **37**, 7242-7251.
26. J. C. Pérez-Flores, Pérez-Coll, D., García-Martín, S., Ritter, C., Mather, G.C., Canales-Vázquez, J., Gálvez-Sánchez, M., García-Alvarado, F., Amador, U., *Chemistry of Materials*, 2013, **25**, 2484-2494.
27. A. Glazer, *Acta Crystallographica Section B*, 1972, **28**, 3384-3392.
28. A. Gómez-Pérez, Pérez-Flores, J.C., Ritter, C., Boulahya, K., Castro, G.R., García-Alvarado, F., Amador, U. , *Journal of Applied Crystallography*, 2014, **submitted**.
29. W. H. Zachariasen, *Acta Crystallographica*, 1963, **16**, 385.
30. K. Robinson, Gibbs, G. V. & Ribbe, P. H., *Science*, 1971, **172**, 567-570.
31. A. E. Miller, Daane, A.H. , *J. Inorg. Nucl. Chem.*, 1965, **27**, 1955-1960.
32. S. V. Ordin, Shelykh, A. I., *Semiconductors*, 2010, **44**, 558-563.